Science Advances
MAAAS

Supplementary Materials for

Persistence of intense, climate-driven runoff late in Mars history

Edwin S. Kite*, David P. Mayer, Sharon A. Wilson, Joel M. Davis, Antoine S. Lucas, Gaia Stucky de Quay

*Corresponding author. Email: kite@uchicago.edu

This PDF file includes:

Supplementary Information

Chronology

Mars terrain ages are estimated by measuring terrain crater density relative to Lunar terrains that have been radiometrically dated using Apollo samples, with a correction for the Moon-to-Mars impact flux ratio. The ages used in this paper, from Michael (2013), are as follows: Late Noachian, 3.85-3.6 Ga; Early Hesperian, 3.6-3.4 Ga; Late Hesperian, 3.4-3.2 Ga; Early Amazonian, 3.2-1.0 Ga; Middle Amazonian, 1.0-0.3 Ga. For terrains too small and/or too heavily modified for crater-age dating to be reliable, crosscutting relationships and the degradation state of sharp topographic features such as the rims of large craters can used to find relative age (e.g. Mangold et al. 2012). Relative stratigraphic ages (e.g. Late Hesperian) are tied to measured crater densities, so the observation that almost all of the rivers in our database formed long after almost all of the diameter >16 km craters on Mars is robust. However, quantitative age assignments are subject to future revision as our understanding of Solar System chronology improves. We use previously published age estimates for Mars terrains that record river flow. The regionally-integrated highland valley networks of Mars formed around the Late Noachian / Early Hesperian boundary, 3.85-3.4 Ga). By contrast, the stratigraphic ages of the channels/fans measured here are mainly <3.4 Ga (Late Hesperian and Amazonian; e.g., Grant & Wilson 2011, Mangold et al. 2012), with most Amazonian channels/fans being Early Amazonian in age (3.0-1.0 Ga). We choose not to subset our geographic clusters (Fig. 1) by age within this range. This is because measuring relative terrain crater density becomes more challenging for smaller count areas, so that (in the absence of dispositive crosscutting relationships) cluster-to-cluster relative age ordination becomes questionable. An exception is Lyot crater's stippled mantle unit, into which the Lyot channels are incised. The Lyot stippled mantle unit, which is likely ice-rich, is Middle Amazonian in age (Dickson et al. 2009), corresponding to 0.3-1.0 Ga according to Michael (2013). Therefore, the Lyot rivers are much younger than most of the other rivers in our dataset (Fig. 5a).

Early papers (e.g. Moore & Howard 2005) considered Mars' alluvial fans to have formed under the same wet climate as the regionally-integrated valley networks. It is now known that most alluvial fans and many deltas significantly postdate the regionally-integrated valley networks (e.g. Grant & Wilson 2011, Mangold et al. 2012, Goudge et al. 2016).

Gale crater (~3.6 Ga), the target of the Mars Science Laboratory investigation, was a late arrival to the densely-cratered Mars landscape: only six Mars craters of similar size are larger (Irwin 2013). Despite this relative youth, Gale is pervasively water-altered (Grotzinger et al. 2015), exemplifying the decoupling of river-forming climates on Mars from the impactor flux.

Previous work.

Although there have been several more recent surveys, the most extensive previous study of runoff production on Mars, and the only one to report a globally-distributed dataset, remains the *n* = 15 runoff-production dataset of Irwin et al. (2005). Using CTX and HiRISE images that were not available in 2005, we were unable to reproduce many of the

measurements of Irwin et al. (2005), which were made using lower-resolution images, mostly from the 18m-per-pixel THermal EMission Imaging System - Visible Imaging Subsystem (THEMIS-VIS). In some cases we found inner channels at the locations reported by Irwin et al., but their width (measured using higher-resolution images than were available in 2005) was a factor of ~2 narrower than reported using lower-resolution images. In other cases, we considered a lake-overspill contribution to be plausible (in which case the channel width does not have to correspond to climate-fed runoff). In a few cases (e.g. Eberswalde; Unnamed_Memnonia_3 from Irwin et al. 2005) we found agreement within 25% between our measurements and those of Irwin et al. (2005). This difficulty does not compromise our conclusion that late-stage runoff production was intense. Figure S7 compares our database to the results reported by Irwin et al. (2005).

Burr et al. (2010) and Kite et al. (2015) report paleodischarge estimates, but (except in one case) they do not report catchment areas.

Details of measurement procedure.
The overall workflow is sketched in fig. S2. The workflow largely followed Kite et al. (2015).

We used the best-resolution images available for each measured channel. Typical channel widths in our database are 50-100m; typical image resolution (most of the stereopairs that we used involved HiRISE 2 × 2 binning) is 0.5 m/pixel (~100 pixels/width). Therefore, features are well-resolved.

Our search for paleo-rivers was guided by a survey for alluvial-fan-hosting craters and delta-hosting craters using CTX images that covered more than ½ of Mars' surface area between 40°S and 40°N (Wilson et al. 2013). Sites outside of the Wilson et al. (2013) catalogue were inspected when they corresponded to an actual Mars rover landing site; corresponded to a site shortlisted for a NASA Mars rover landing (e.g. SW Melas Chasma); were included in a catalog of glacier-associated channels given to us by C.I. Fassett (NASA MSFC, via email); were listed in Table 1 of Irwin et al. (2005); or were documented for Lyot crater by Dickson et al. (2009). Some paleo-rivers are found N of 40°N and S of 40°S, including the Lyot channels (Dickson et al. 2009) which are included in our survey. Not all inspected sites yielded data points, because of our restrictive quality criteria. Moreover, additional alluvial fans and deltas have been discovered on Mars beyond those listed in the Wilson et al. (2013) catalogue - and HiRISE imaging of paleo-river sites that are ill-resolved in CTX continues apace. No survey using HiRISE images can be homogenous because HiRISE images are targeted on the basis of features that appear most interesting in lower-resolution images, and HiRISE footprints cover only ~2% of the planet's surface area. For these reasons, we expect that a hypothetical future global survey would find additional well-preserved paleo-rivers beyond those plotted in Fig. 1.

Widths and wavelengths. Channel centerlines (for sinuous segments of channel where channel centerlines were well-preserved), and also channel margins (for segments of channel where channel margins were well-preserved), were traced in ArcGIS. As for

paleochannels on Earth, the quality of preservation varies along channel. Moreover, as for channels on Earth, river width varies along-channel. We measured only the best-preserved segments for each measured paleochannel. To ensure measurement repeatability, channel centerlines for meander wavelengths were measured in triplicate, blind to previous measurements. Image orientation was rotated by 90 degrees for each channel-centerline trace to minimize perceptual errors correlated with apparent lighting angles.

For channel width variations, in cases where only one channel segment is measured, we report the standard deviation of the channel width as the error bar. Because the MATLAB code uniformly dots along the channel banks, the width estimate is not biased by the distance between hand-picked points. Where best-preserved segments were discontinuous along a channel, we weighted each segment equally to get the channel average. Where multiple channel segments are measured, we report the standard deviation between channel segment central estimates as the error bar. Confusion due to vertical and horizontal amalgamation of channels in outcrop was minimized by inspection of the best available DTMs and anaglyphs.

Widths and wavelengths were extracted automatically in MATLAB (figs. S2c & S2d), following Kite et al. (2015). All channel traces were reprojected in MATLAB to a stereographic projection with center longitude equal to a representative longitude of the channel trace. Second-order projection distortions are very small, and so were not corrected. Centerline traces were done in triplicate. The main free parameters in the automatic extraction algorithm are the smoothing wavelength for inflection identification (~100 m, smaller for shorter traces) and the minimum sinuosity (set to 1.1). Only half-meanders that had minimum sinuosity >1.1 in two or more traces were considered. Errors are aggregated on a per-channel basis. The entire output of the code was checked by visual inspection. In a few cases, the code did not pick a half-meander because the smoothing washed out the inflection point. In these few cases, we added an inflection point "by hand" to the trace in order to force the code to pick a half-meander. In one case, the code picked the incorrect width for a channel due to a single incorrectly-traced vertex. In that one case, we removed the incorrectly-traced vertex.

In most cases, segments of channel with well-preserved channel margins did not overlap with segments of channel with sinuosity >1.1.

Areas. Area measurement was done by manually delineating polygons roughly perpendicular to contour lines on the best-available DTMs, interpolated across young craters for the catchments of the oldest rivers. Bias was towards using the largest reasonably possible catchment area, which means that we tend to underestimate runoff production, which is conservative for the purposes of this paper (higher runoff production would strengthen our conclusions). For alluvial fans, we considered the alcoves upstream of the fan apex to be the sole runoff source. This is because the absence of evidence for channel heads on the alluvial fans themselves suggests that the alcoves upstream of the fan apex are the sole water source for the alluvial fans (Moore & Howard 2005). Real catchments generate runoff from only a small part of

the catchment, so our use of the topographic catchment area will tend to further understate the true maximum in runoff production.

Slopes. One of our paleodischarge estimation methods uses slope measurements. Slope measurements were made using the best available DTMs on modern topography. Due mainly to limited DTM precision, 8/205 (4%) of width data had negative or zero slopes for the widths. We set these to a very small slope (10^{-3}, ~0.05°) for fitting. The modern slope can differ from the paleo-slope, in principle. That is because the paleo-slope might be altered by differential compaction (Grotzinger et al. 2015) as well as by differential erosion. In practice, differential compaction of late-stage fluvial deposits is uncommon, perhaps because of a combination of coarse grain sizes (gravel) and low gravity. Although wind erosion tends to erode the toes of alluvial fans more than the apices of alluvial fans, the wind-erosion depth is small compared to the thickness of the fans. Therefore, the corresponding slope error is small, except for a few sites in the SE of Roddy crater. Slopes are not corrected for channel sinuosity, but because channel sinuosity is usually low (Fig. 2b) the corresponding error is small.

Latitudes. The present-day latitudes of the Mars rivers are a good proxy for their formation latitude, because Hesperian/Amazonian Mars lacked plate tectonics, and there is little evidence for large-amplitude Hesperian/Amazonian polar wander.

Getting from orbital images of ancient sediments to past channel bankfull width.

A candidate terrestrial analog to the inverted channels of Mars is located near Green River in SE Utah (38.8°N 110.3°W). At this site, sinuous ridges preserve channel deposits and point-bar deposits (Williams et al. 2009). Paleodischarge Q estimated using channel width alone is about a factor of 2 higher than paleodischarge estimated using methods including slope and grainsize information (Williams et al. 2009). At this site, channel deposits preserved within sinuous ridges can be less than the width of the flat top of the ridge, and in some interpretations the width of the flat top of the ridge corresponds to channel-belt width, not a channel width (Nuse 2015). These Earth-analog data are a warning against over-interpreting HiRISE DTMs, in part because grain-size and bedset-thickness measurements are very difficult to make from orbiter data. For many Mars river deposits, the simplest interpretation of sinuous-ridge width is nevertheless that ridge-top width corresponds to inverted channel width. This is because of the following factors: (1) sandblasting-away of floodplain deposits. This allows diagnostic bedforms, e.g. lateral-accretion deposits, to be recognized from orbit much better than on Earth, where erosion is by processes that are much less sensitive to target grain size than is the sandblasting process (fig. S1); (2) agreement between meander-wavelengths and paleochannel widths, which allows cross-checking (Fig. 2); (3) preservation in some cases of channel banks as ridges, due to increased cementation of the channel banks; (4) rivers can transition from negative-relief valley floors to positive-relief channel floors, which arguably decreases the likelihood that either is an artifact (fig. S1; Davis et al. 2016).

Getting from bankfull width to paleo-runoff production.

We used the following equations (SI units).

(1) For the threshold channel approach, we used the approach of Dietrich et al. (2017), as follows. For river bankfull depth H,

$$H = 0.15 \, S^{-0.75} \, P \, D_{50};$$

with P (specific gravity) = 1.9. Gravity does not appear in this expression, because the submerged weight of the sediment grains cancels the reduced shear stress of the water. Mean bankfull flow velocity is given by the Darcy-Weisbach relation,

$$u = k_{DW} \, (g \, H \, S)^{0.5}$$

where we set

$$k_{DW} = 17.7 \, (H/D_{84}) \, (56.3 + 5.57*(H/D_{84})^{5/3})^{-0.5}$$

with $D_{84} = 2 \, D_{50}$ (Dietrich et al. 2017). (We also used the relation $D_{84} = 2 \, D_{50}$ to convert from the D_{84} estimate of Morgan et al. 2014 to the dark-gray D_{50} band plotted in Fig. 3). Finally,

$$Q = w \, u \, H.$$

(2) For the gravity-corrected empirical width-discharge relationship (Kite et al. 2015):

$$Q_w = (w/(1.257 \times 3.35))^{1.8656}$$

(3) For the gravity-corrected empirical wavelength-discharge relationship (Burr et al. 2010, Kite et al. 2015):

$$Q_\lambda = 0.011 \times (\lambda./1.267)^{1.54}$$

At present there is no general mechanistic theory for the width of river channels (e.g. Parker et al. 2007, Pfeiffer et al. 2017) that applies for Mars. We used Eqns. (13) and (14) of Parker et al. (2007) to predict D_{50} and Q for our Mars channels, using W and S as inputs. We found that relationships among slope, grain size, and bankfull hydraulic geometry that have been proposed to be quasi-universal on the Earth (e.g. Parker et al. 2007), when applied to Mars, predict large grain sizes (> 1m) that are not observed in HiRISE images. Therefore the Parker et al. (2007) Earth relations cannot be fully valid for Mars rivers. We speculate that this inapplicability is causally connected to the steep slope-area relation of Mars channels, relative to Earth channels (fig. S4).

<u>No evidence for a permafrost effect in (bankfull width)-(bankfull discharge) relationships for Earth rivers.</u> It is possible that Mars rivers formed in permafrost. If so, Earth scalings built on data gathered from permafrost-free rivers might not be applicable. To check for a

permafrost effect in the hydraulic geometry of Earth rivers, we analysed the USGS HYDRoacoustic dataset in support of the Surface Water Oceanographic Topography satellite mission (HYDRoSWOT; Canova et al. 2016). This data set aggregates channel and flow data collected from the USGS streamgaging network, including discharge and water-surface width. We found that for the 22 unique latitudes >67°N in the database, all of which are located in Alaska, the best-fit discharge (for a given water-surface width) differs by <10% relative to the average discharge for the entire 2×10^5 - measurement dataset. This shows that rivers with latitudes >65°N in the HYDRoSWOT database have a width-discharge relationship that is not greatly different from the width-discharge relation in the database as a whole.

Getting from paleo-runoff production to paleoclimate implications.

Regional Variations. The k-means clustering algorithm uses longitude and 1.6 × latitude as inputs but wraps around the 180°E line. This yields more geologically meaningful clusters than wrapping on the 0°E line. The cluster break at the 0°E line that is visible in Fig. 1 occurs for both cases. We used the factor-of-1.6 boost to the latitude before input to the k-means algorithm in order to generate clusters that (in our judgment) were more geologically meaningful.

Regional variations are less significant than the global trends of (i) large channels that (ii) increase in size with area less rapidly than on Earth. The area around the Mars Science Laboratory rover landing-site - the Gale-(Aeolis Planum)-(Zephyria Planum) region, region 4 in Figs. 1 and S6 - plots low in fig. S6. However, we do not consider this tendency to be significant in our dataset. This is because of (1) the small number of data points (n = 33) combined with geologic noise, and (2) the greater availability of high-resolution images near the Mars Science Laboratory landing site, so that small channels are better recorded here. All but one of the smallest (<10 km²) catchment areas drain layered sediments in SW Melas Chasma (Davis et al. 2018). Those layered sediments are interpreted as atmospherically-transported sediment. If they are atmospherically-transported sediment, then the correspondingly small grain size would tend to produce wider channels for a given paleodischarge.

Discharge-area scaling. Paleodischarge fits suggest that river discharge does not increase as quickly with catchment area on Mars than it does on Earth (fig. S5). Why is this? Possibilities include the following. (i) Non-detection or geologic destruction of the smallest rivers, leading to a bias towards finding relatively large rivers in the smallest drainage-area bins. This is plausible because, although the smallest rivers are well-resolved in HiRISE images, those HiRISE images are targeted on the basis of river detections in lower-resolution images. (ii) If the $Q(A)$ distribution is the same, then rivers must get deeper with area more quickly than on Earth. This means that the grain size does not get smaller as quickly on Mars than on Earth (i.e., less efficient downstream fining on Mars). (iii) Shorter-duration runoff events on Mars than on Earth: this is unlikely however, given the large catchment areas involved. (iv) Runoff on Late

Hesperian / Early Amazonian Mars that had more within-catchment spatial patchiness than on Earth.

Relationship between runoff production and paleotemperature. In snowmelt climates, the 1 hour runoff-production will not exceed ~3 mm/hr. In the warmer, rainfall climates of the contiguous United States, the 1 hour annual-maximum runoff-production rate (relevant to flash-flooding in basins on $O(10^1)$ km^2 scales) is ~10 mm/hr for the Basin & Range and >30 mm/hr for Tornado Alley (Grim & Pinto 2011).

In most cases, we can be confident the late-stage Mars rivers are not the result of the direct energy impact of an asteroid or comet. Flash-melting of snow or ice due to reentry heating from distal impact ejecta can be rejected as an explanation for most of the post-3.6 Ga data, because the cumulative melting from this mechanism cannot move enough sediment to explain the observed km-thick deposits (Kite et al. 2017). For two sites in our Mars database (22°N 176°E and 9°N 34°W), our interpretation of the geologic relations suggests a possible localized impact trigger for the precipitation. At a few other sites, detailed energy balance calculations and geologic mapping would be needed to test the hypothesis of a localized impact trigger.

Eskers on Mars are less common than inverted channels on Mars. Most of the sinuous ridges in our database also lack the associated glacial landforms that might be expected to be found with eskers. For Chukhung crater (region 6 in Fig. 1), it is possible that some of our measured sinuous ridges may be eskers. Region 6 plots below the planetary runoff-production trend (fig. S6), so removal of these data would not affect our conclusions.

Table S1. Table of DTMs. 49% of data were gathered with the aid of HiRISE anaglyphs. All DTMs are available for unrestricted further use. To obtain UChicago DTMs, contact the lead author. To obtain DTMS produced by J.M.D., go to https://doi.org/10.6084/m9.figshare.c.4119992. (*) DTM stored at UChicago, but produced by E.S.K. at SETI Institute.

Source of DTM	Stereo pair
HiRISE DTMs produced for this study, UChicago (D.P.M.)	ESP_033108_1800_ESP_033253_1800
	ESP_017477_2190_ESP_018545_2190
	ESP_016260_2295_ESP_016339_2295
	ESP_029221_1565_ESP_028799_1565
	ESP_037093_1570_ESP_036526_1570
	ESP_032159_1755_ESP_032370_1755
	ESP_040097_1760_ESP_039675_1760
	ESP_030880_1750_ESP_030102_1750
	PSP_002464_1745_PSP_003176_1745
	ESP_019489_1510_ESP_025291_1510
	ESP_039889_1565_ESP_040522_1565
	ESP_030814_1750_ESP_030748_1750
	ESP_019035_2165_ESP_018178_2165
	ESP_046350_1515_ESP_046205_1515
	ESP_037093_1570_ESP_036526_1570
	PSP_007543_1580_PSP_007899_1580
	ESP_025828_2030_ESP_025973_2030
	ESP_038530_1830_ESP_038398_1830
	ESP_018738_1585_ESP_019160_1585
	ESP_029221_1565_ESP_028799_1565
	PSP_006528_1585_PSP_007095_1585
	ESP_032159_1755_ESP_032370_1755
	ESP_042368_1580_ESP_042869_1580
	PSP_002464_1745_PSP_003176_1745
	ESP_022140_1585_ESP_021784_1585
	ESP_030814_1750_ESP_030748_1750
	ESP_019035_2165_ESP_018178_2165
	ESP_016260_2295_ESP_016339_2295
	ESP_016039_1560_ESP_016540_1560
	PSP_007688_1575_PSP_008545_1575
	PSP_009623_1755_PSP_007975_1755 (*)
HiRISE DTMs produced by UCL (J.M.D.)	ESP_012493_1700_PSP_005663_1700
	ESP_013983_1705_ESP_013561_1705
	PSP_005874_1700_PSP_005452_1700
PDS DTMS (publicly available)	PSP_008379_1700_PSP_007377_1700
	PSP_001336_1560_PSP_001534_1560
	ESP_025625_1580_ESP_024913_1580
	PSP_009650_1755_PSP_009716_1755
	ESP_020324_1555_ESP_020390_1555
	PSP_009025_1705_PSP_008669_1705

Table S2. Geologic settings of study sites. *Table notes.* 1. We interpret these channels as having been incised into debris cover over fairly pure ice, based on previously-published data. 2. Geographic region with unusual preservation style (Davis et al. 2018). 3. An unusually large river preserved in inverted relief. One data point for widths (0.49%, which rounds to 0%).

Geologic setting:	Width measurements (*n*=205)	Wavelength measurements (*n*=104)
	% of total	% of total
Channel within sediments/sedimentary rock:	*87*	*85*
Alluvial fan	54	31
Deltaic	1	4
Sedimentary mound	0	1
Canyon fill	1	1
Crater fill	9	16
Glacier-associated[1]	7	17
SW Melas canyon interior[2]	14	12
Aeolis Serpens[3]	0	2
Channel within ancient crustal materials:	*13*	*15*
Highlands	13	13
Crater ejecta	0	2

High-preservation-quality example. 138.07°E 5.63°S / HiRISE. Paleoflow from top to bottom. Channel deposit transitions from inverted relief (bottom) to negative relief (top). Channel is 35-40m wide. Note that banks appear to be preserved differently from channel fill.
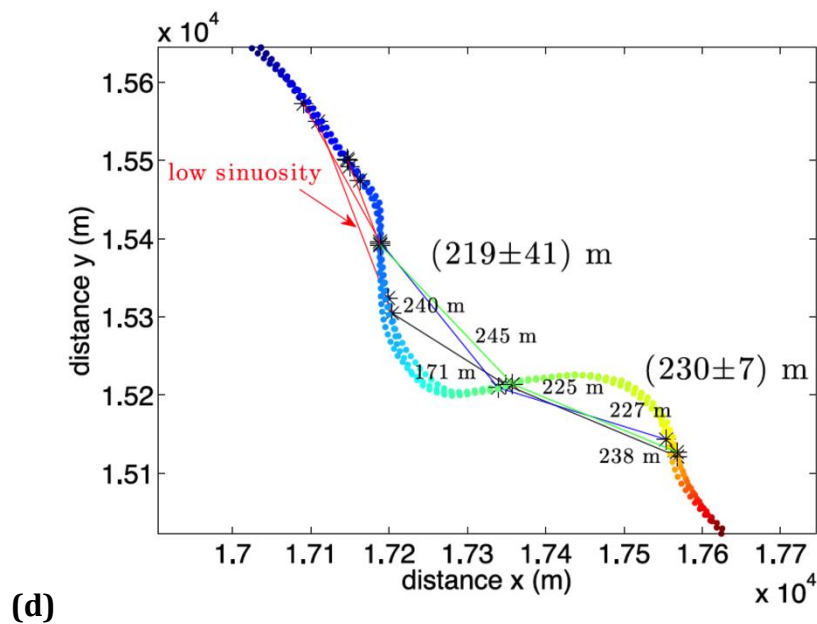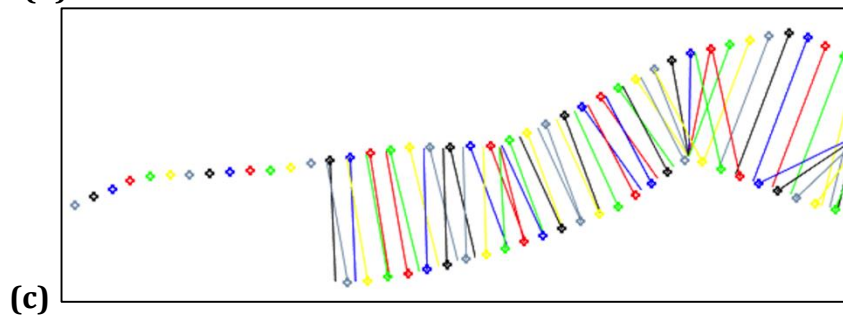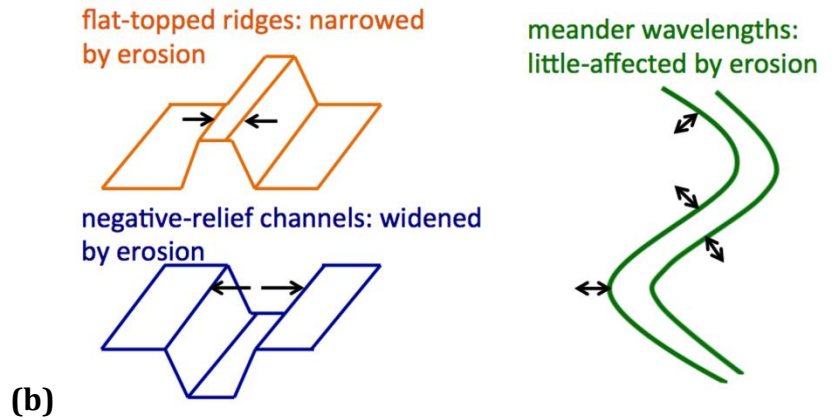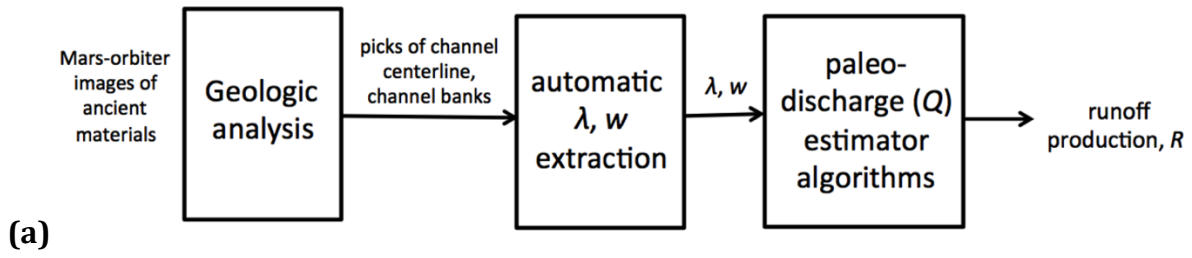

Good-preservation-quality example. Alluvial fan apex (Peace Vallis, upstream of the Mars Science Laboratory "Bradbury" landing site) / HiRISE. Channel is ~74 m wide. Paleoflow to lower right.


Example of relatively low-quality ("probable") preservation of channel width. HiRISE DTM. Channel ~55-60m wide 138.148°E 5.546°S (Gale Crater). Paleoflow from top to bottom.
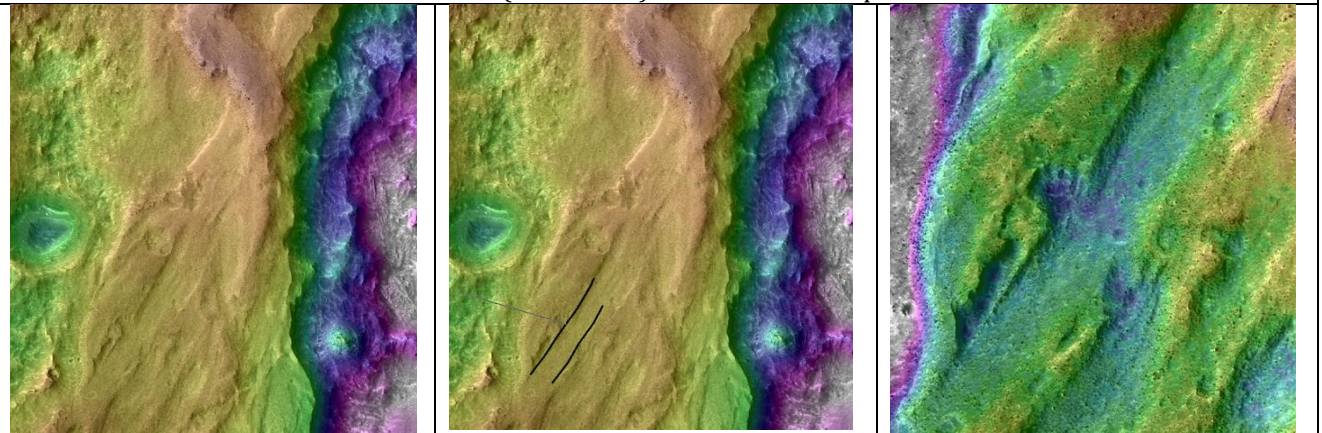
Fig. S1. Examples of traces showing preservation quality. Left column shows representative images, center column shows interpreted channel banks (black trace), and right column shows a zoom on area of interest.

(a)

Mars-orbiter images of ancient materials → Geologic analysis → picks of channel centerline, channel banks → automatic λ, w extraction → λ, w → paleo-discharge (Q) estimator algorithms → runoff production, R

(b)

flat-topped ridges: narrowed by erosion

negative-relief channels: widened by erosion

meander wavelengths: little-affected by erosion

(c)

(d)

x 10⁴

low sinuosity

(219 ± 41) m

240 m

245 m

171 m

225 m

(230 ± 7) m

227 m

238 m

distance y (m)

distance x (m)

x 10⁴

Fig. S2. Details of method. (a) Overall workflow. **(b)** Cartoon to show how erosion affects channel dimensions. **(c)** Example of channel width extraction. Points are automatically dotted along either manually-traced channel bank. Lines are drawn to the closest point on the opposite bank, ignoring bank end-points. The reported channel width is the median of the resulting widths. **(d)**. Example of wavelength (λ) extraction from repeated ArcGIS traces (this figure is a reproduction of Fig. 3 from Kite et al., 2015). Points are uniformly interpolated along three independent centerline traces (colored dots). Dot color corresponds to the modern topographic range – standard deviation of 4 m in this case. Lines link inflection points (asterisks) that are obtained from each centerline trace. The low-sinuosity half-meander (arrowed) is excluded from the analysis.

(a)

(b)
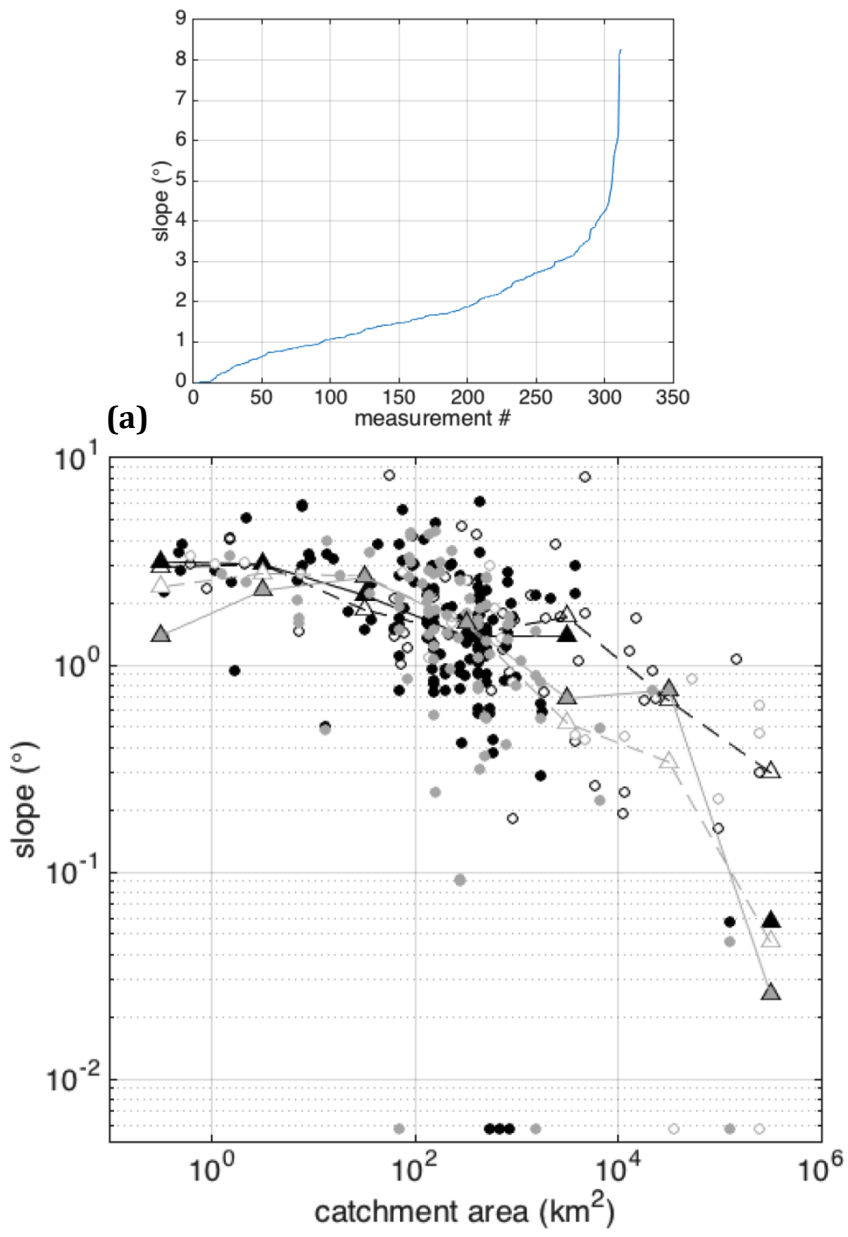
Fig. S3. Paleo-river slope data. (a) Slopes of channels at sites of channel width measurement. The channels are too shallow to be debris-flow chutes. Note that any individual measurement has considerable uncertainty, due to errors associated with measurement and non-uniform erosion. 4% of measurements had slopes that were either indistinguishable from zero or were back-tilted relative to the downslope inferred from regional geology/geomorphology. These had slope set to 0.05° for calculations.
(b) Slope-area relationship for our Mars database. Black = widths; gray = wavelengths. Triangles = averages, defined using catchment-area bins spaced by of a factor of 10 in catchment area. For each data point, the slope is measured using the terrain model with the best-available resolution (HiRISE DTM favored over CTX DTM; CTX DTM favored over MOLA). Solid lines and filled symbols correspond to slopes measured using CTX DTMs

and HiRISE DTMs. Dashed lines and open symbols correspond to slopes measured on the basis of all data sources (MOLA, CTX DTMs, and HiRISE DTMs).


(a)

(b)
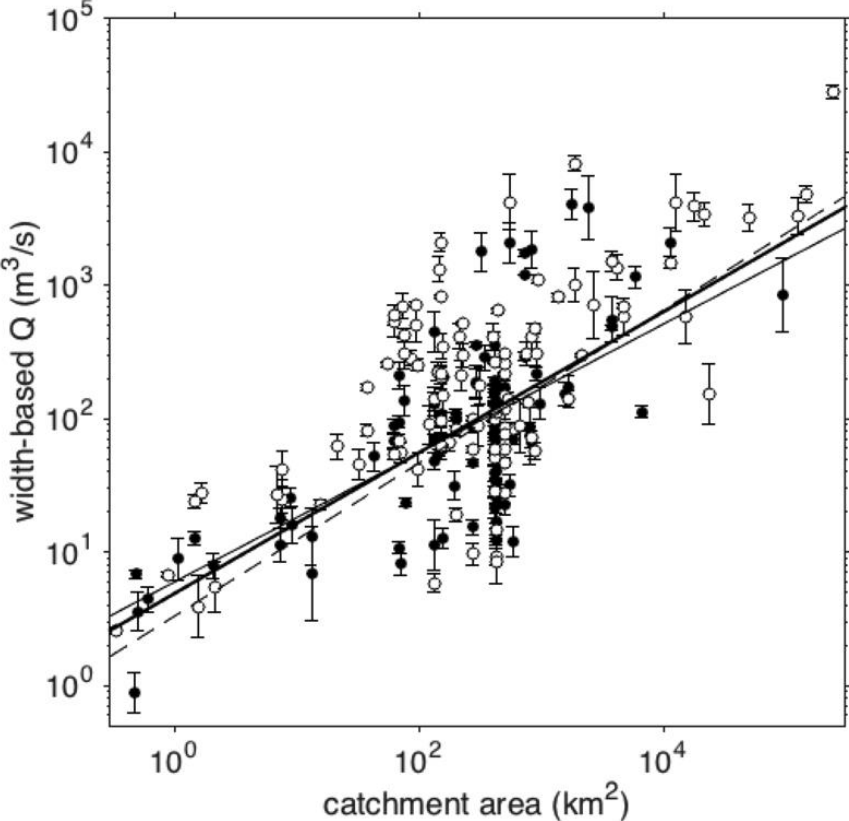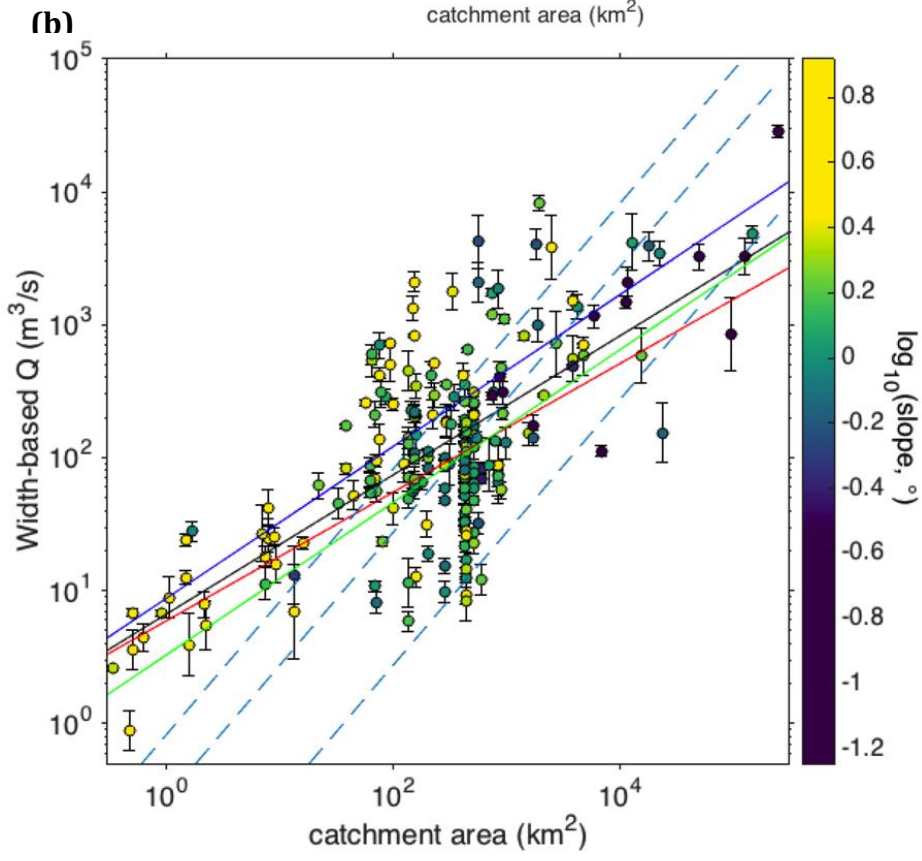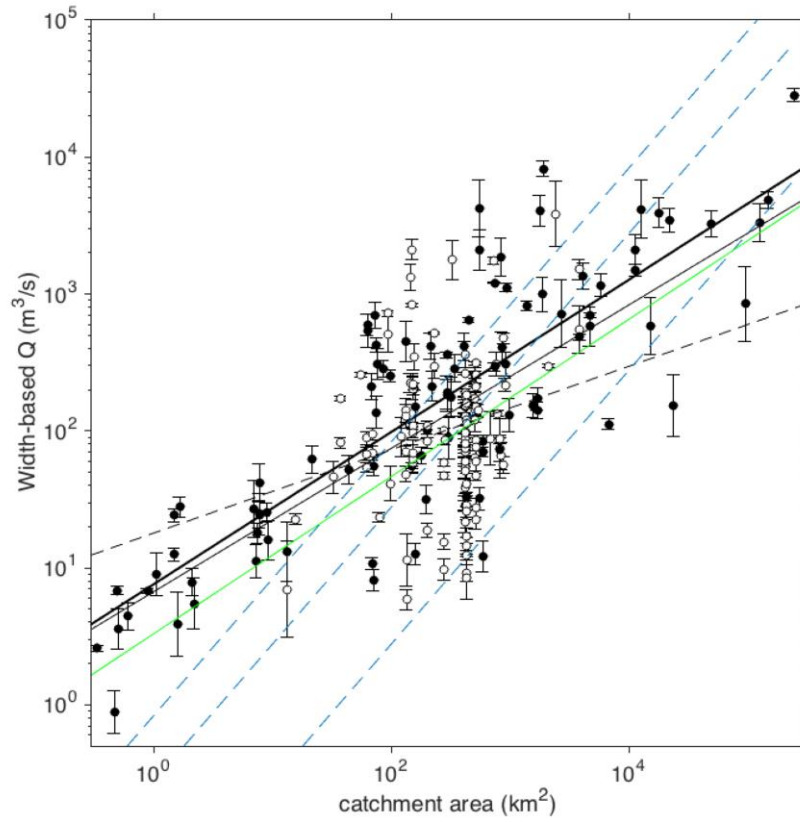
(c)

Fig. S4. Sensitivity tests. The dashed blue lines in panels (b) and (c) correspond to catchment-averaged inferred runoff production of (from bottom) 0.1 mm/hr, 1 mm/hr, and 3 mm/hr. **(a)** *Preservation quality.* The best-fit discharge-area relation fitting only to the best-preserved river widths (closed dots for data, thick solid line for fit; *n* = 97) is the same within error as the best-fit discharge-area relation fitting only to the relatively-poorly-preserved river widths (open dots for data, thin solid line for fit, *n* = 108). The best-fit discharge-area relation for meander wavelengths is shown by the dashed line. **(b)** *Effect of removing all alluvial fan data.* Thin solid line is the fit to all width data, thick solid line is the fit to width data with points from the alluvial fan geologic setting excluded, and thin dashed line is the fit to data from the alluvial-fan geologic setting alone. Open circles = width-based discharge estimates for widths corresponding to the geological setting "Alluvial fan". Filled circles = width-based discharge estimates for widths from other geological settings (listed in Table S2). The green line shows the fit to the sinuous-channel wavelength data. **(c)** *Effect of slope on width-inferred paleodischarge.* The black line shows the fit to the width data, the red line shows the fit to the inverted-relief channels only, the blue line shows the fit to the negative-relief channels only, and the green line shows the fit to the sinuous-channel wavelength data. Filled circles correspond to paleodischarge inferred from width data, with the fill color corresponding to the slope for that paleochannel. Steep slopes (bright fill colors) plot at larger width for a given area than do shallow slopes (dark fill colors). Possible explanations include the following. (1) Inverted-relief channels are preserved preferentially on shallower slopes (Fig. 2). Because inverted-relief channels tend to be narrowed by erosion (fig. S2), shallower slopes preserve smaller widths. (2) Rivers adjust to a depth that is marginally sufficient to transport bedload. In this picture, steeper rivers can transport sediment at a shallow depth, so if paleodischarge is a function of area only, then river depth is smaller and river width is larger for steeper slopes.
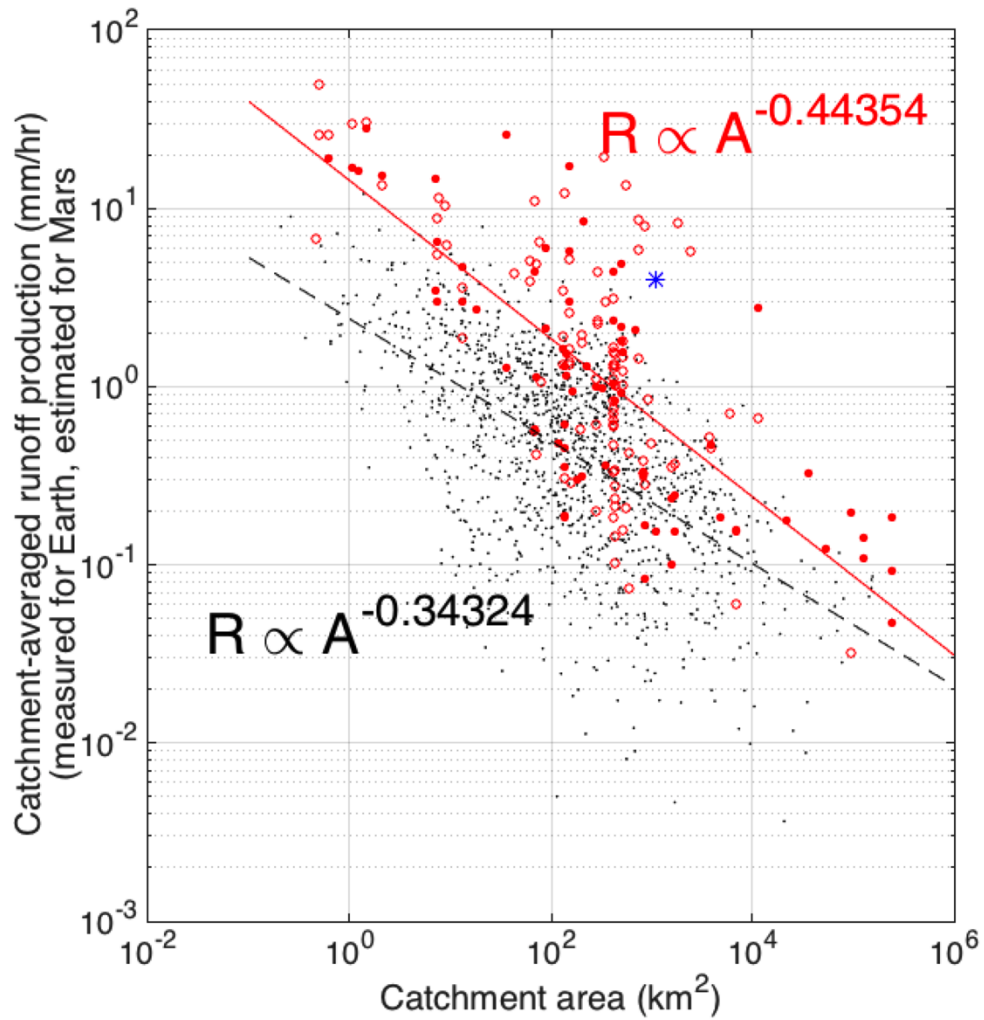
Fig. S5. Discharge area scaling: Relationship between catchment-averaged runoff production, *R*, and drainage area, *A*. Catchment-averaged runoff production is calculated on the basis of gage data for Earth data (black dots correspond to data; black dashed line corresponds to best fit). Catchment-averaged runoff production is inferred on the basis of widths and wavelengths for Mars paleo-rivers. Specifically, open red circles are runoff production inferred using empirical method from better-preserved Mars widths, filled red disks are runoff production inferred using better-preserved Mars wavelengths, and the solid red line corresponds to best fit for Mars data. Blue asterisk corresponds to the 2013 Boulder, Colorado flood.
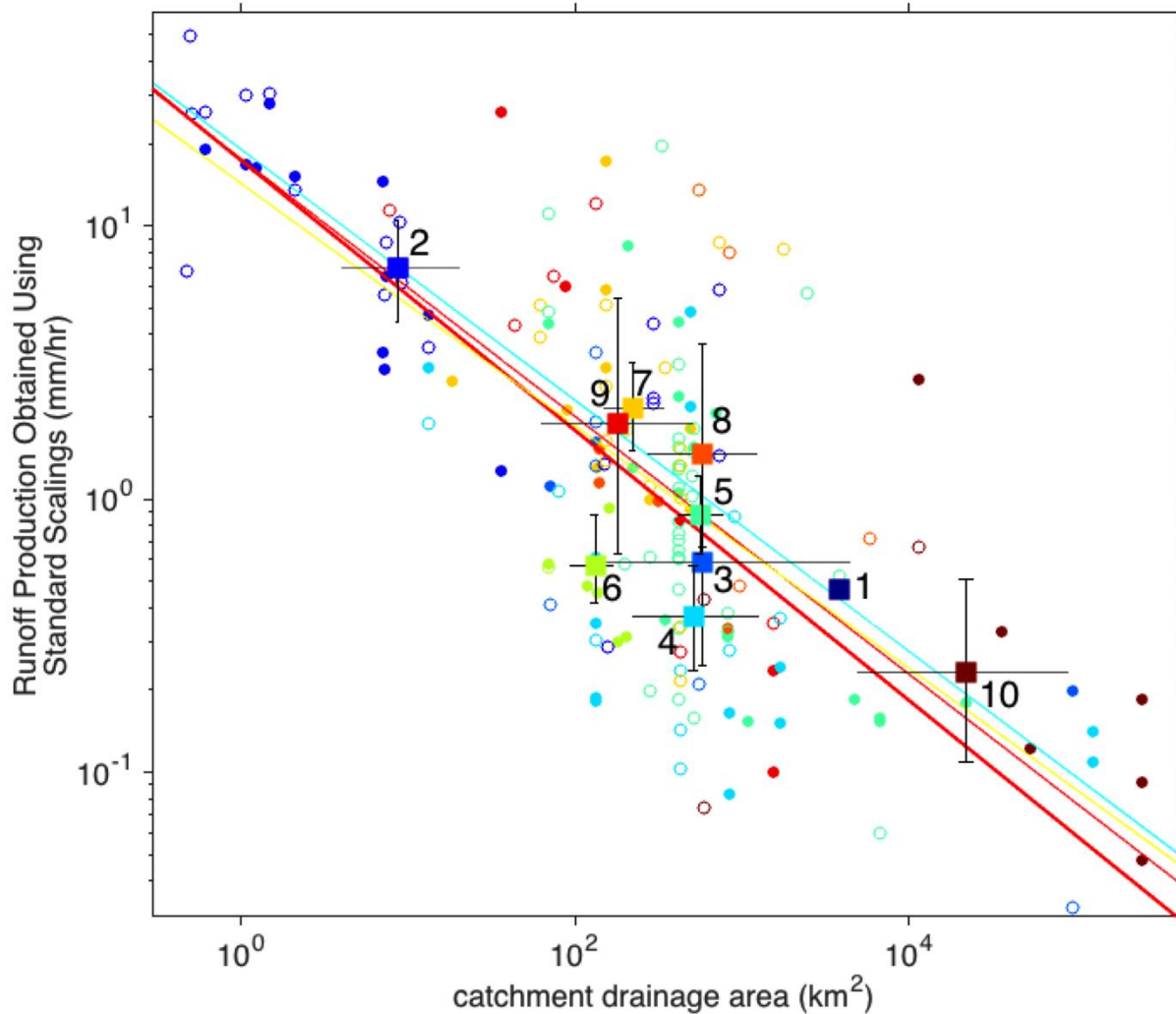
Fig. S6. Regional variations in estimated runoff production. Colors and numbers map to symbols and geographic clusters shown in Fig. 1. Filled disks correspond to runoff production inferred on the basis of meander wavelengths. Open disks correspond to runoff production inferred on the basis of channel widths. Only the best-preserved widths and wavelengths are shown (all channels in a catchment). Filled squares correspond to geographic-cluster averages, with the error bars corresponding to the bootstrapped 2σ Poisson error for those regional averages. Catchment area is the most significant, and perhaps the only significant, geologic control on regional variation in estimated runoff production in this dataset (see main text). Empirical discharge-width and discharge-wavelength relations are used. The colored lines correspond to best fits, showing the insensitivity of the trends to the quality 'cut' and to the data selection. To show the insensitivity of the results to the inclusion versus exclusion of less-well-preserved channels, the thin cyan line corresponds to the fit using all data; the thin yellow line corresponds to the fit using only the best-preserved widths and wavelengths; the thin red line corresponds to the fit using only the best-preserved widths; and the thick red line corresponds to the fit using only the best-preserved wavelengths.
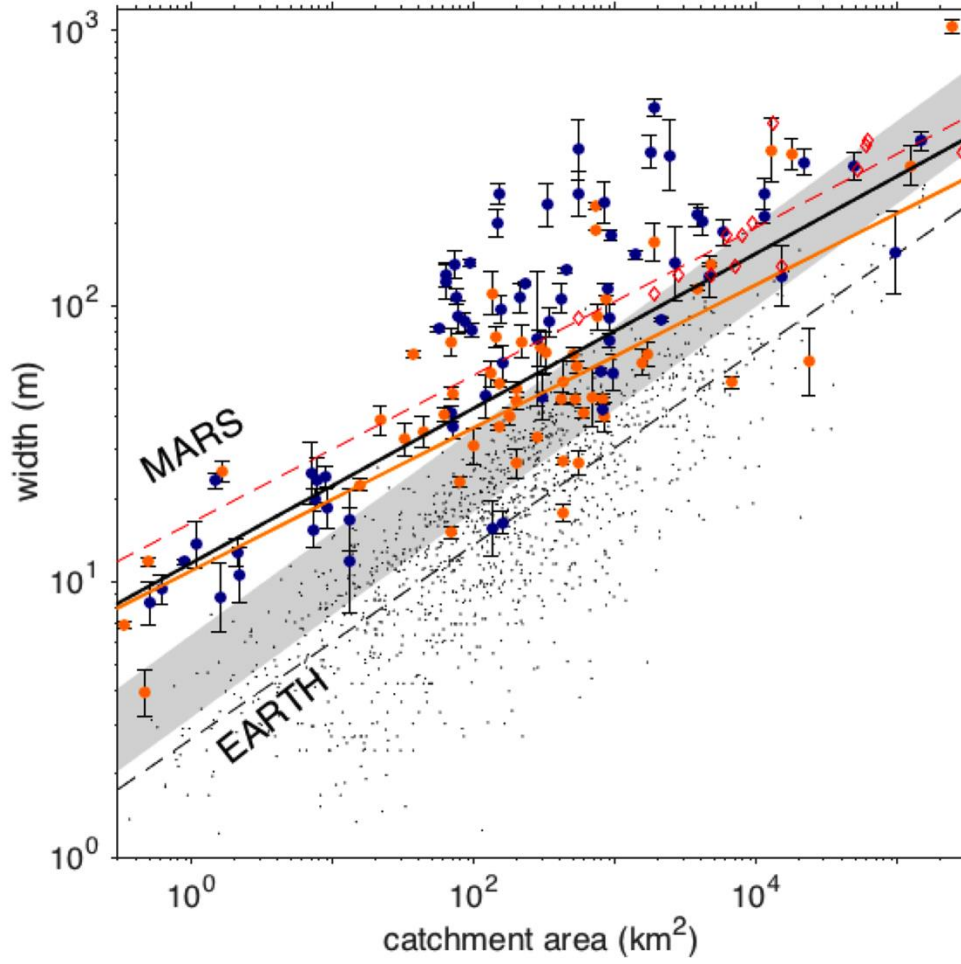
(a)
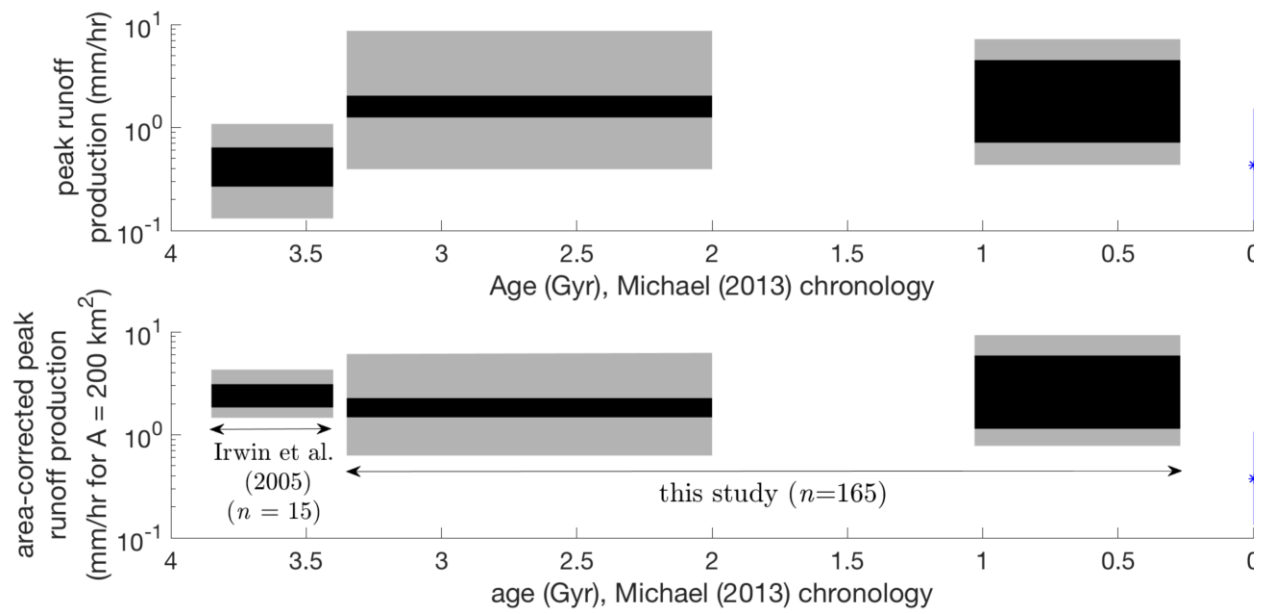
(b)

Fig. S7. Geologic history of Mars' river runoff. (a) Irwin et al. (2005) data (red diamonds and dashed red line for best fit), which correspond primarily to Noachian / Early Hesperian terrains, compared to our measurements. Our Mars data are shown using colored symbols (blue squares=negative relief channels; orange circles=inverted relief channels). The thick black line is the best fit to our Mars data, and the thick orange line is the best fit to our Mars inverted-relief channel widths. Only the widest channel for each catchment area is shown. The gray shaded region corresponds to the channel widths expected based on the best-fit to meander wavelengths (0.0625-0.125× wavelength; Burr et al. 2010). Earth data (Bieger et al. 2015) are shown as black dots and the best-fit to Earth data is shown by the thin dashed line. In order to emphasize trends with age, the 13% of our measurements with geologic setting of "highlands" has been removed, so that the 87% of our measurements that are plotted are overwhelmingly Late Hesperian / Amazonian in age. The Irwin et al. (2005) data fall along the trend of decreasing runoff production with increasing drainage area found in our measurements. **(b)** *Top panel:* Runoff production uncorrected for the effect of drainage area on runoff production, copied from Fig. 5a. This uncorrected runoff production is higher for Late Hesperian / Amazonian data points. Symbols are described in Fig. 5 and are the same as in the bottom panel. *Bottom panel:* Runoff production corrected to a constant drainage area of 200 km^2 using our best-fit discharge-area relationship (Fig. 3). Our data are evidence that high rates of peak runoff production, and thus high rates of landscape erosion via fluvial sediment transport, were sustained after 3.4 Ga. The gray patches correspond to the catchment-to-catchment standard deviation of the estimated runoff production, and the black bars correspond to the bootstrapped 2σ Poisson error for those averages. Only the largest channels for each catchment are included. The left-most bar corresponds to results previously reported by Irwin et al. (2005). The central bar corresponds to our data for Late Hesperian and (Early) Amazonian terrains (with "highlands" measurements excluded). The rightmost bar corresponds to our data for the Middle Amazonian stippled mantling unit of Lyot crater (region 8 in Fig. 1). The offset between Earth runoff production (blue symbols) and Mars runoff production is sensitive to the assumed grainsize (Figs. 3-4).
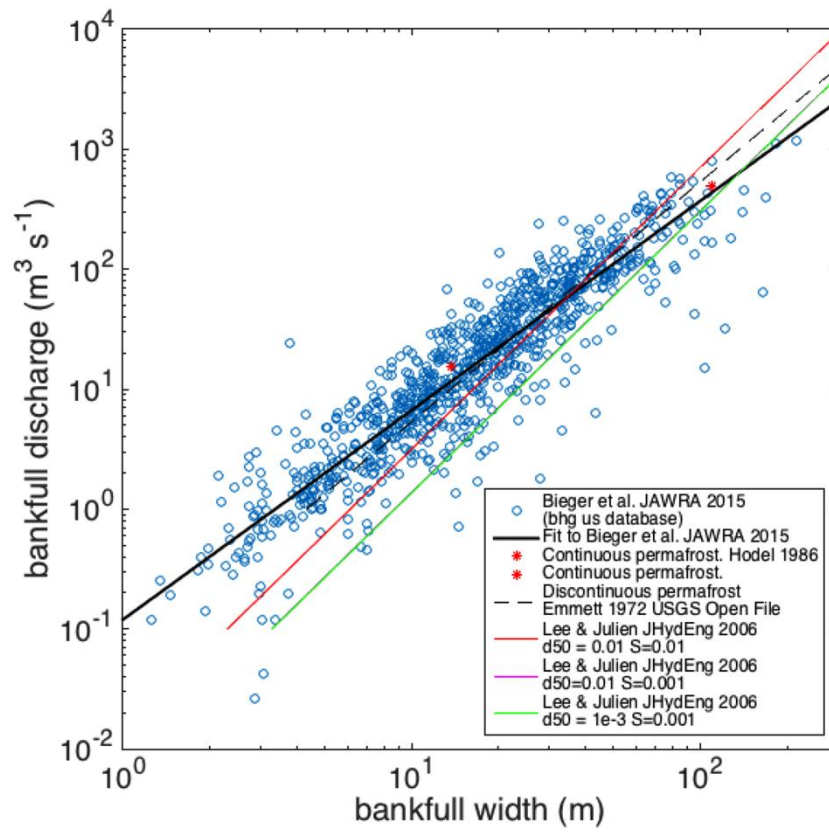
Fig. S8. Width-discharge relationships from terrestrial fieldwork and laboratory experiments. The open blue circles and the solid black line are for the Bieger et al. (2015) dataset. The dashed black line and the red asterisks correspond to measurements from permafrost-affected rivers. The Lee & Julien (2006) data are for constant slope (S, dimensionless) and constant grain size ($d50$, meters). The red, magenta, and green lines correspond to the fits to the Lee & Julien (2006) data recommended by Lee & Julien for different values of $d50$ and S. Natural rivers have a discharge that increases more gradually with width than predicted by the Lee & Julien (2006) fits. This is because of the combined effects of downstream fining and of concavity (shallower slope with increasing downstream distance, and thus width) for stream long profiles in natural rivers.